

# Novel Structural Characterisations of Insulating and Electron Beam Sensitive Materials Employing Low Voltage High Resolution Scanning Electron Microscopy

Osamu Terasaki<sup>1,2</sup>, HaeSung Cho<sup>1</sup>, Minhyung Cho<sup>1</sup>, HuYoung Jeong<sup>1</sup>, Shunsuke Asahina<sup>3</sup>, Yusuke Sakuda<sup>3</sup>, Mituo Suga<sup>3</sup>, Hiroyoshi Kazumori<sup>3</sup>, Masato Kudo<sup>3</sup>, Takeshi Nokuo<sup>3</sup>, Zheng Liu<sup>4</sup>, Sam M Stevens<sup>5,6</sup>, Michael W Anderson<sup>6</sup>, Diana Carolina Galeano Nunez<sup>7</sup>, Ferdi Schüth<sup>7</sup>, Tomas Kjellman<sup>8</sup>, Viveka Alfredsson<sup>8</sup>, Lu Han<sup>9</sup>, Shunai Che<sup>9</sup>, Hexiang Deng<sup>10</sup>, Omar Yaghi<sup>10</sup>, Kanghee Cho<sup>11</sup> and Ryong Ryoo<sup>11,12</sup>

<sup>1</sup> Grad School of EEWS, KAIST

<sup>2</sup> MMK, EXSELENT, Stockholm Univ

<sup>3</sup> JEOL Ltd.

<sup>4</sup> Nanotube Research Center, AIST

<sup>5</sup> Private Contributor

<sup>6</sup> School of Chem, Univ of Manchester

<sup>7</sup> Max-Planck-Inst für Kohlenforschung, Mülheim

<sup>8</sup> Dept. Physical Chemistry, Lund Univ

<sup>9</sup> School of Chem & Chem Eng, Shanghai Jiao Tong Univ

<sup>10</sup> Dept of Chemistry, UCB

<sup>11</sup> Center for Nanomaterials and Chemical Reactions, IBS

<sup>12</sup> Dept of Chem, KAIST, Korea

---

Following our previous appraisal of high resolution scanning electron microscopy (JEOL News 50<sup>th</sup> Anniversary Issue) we return to assess the increasing information from *nano materials* (mesoporous materials, zeotypes, MOF and core-shell materials) delivered to the microscopist through utilisation of scanning electron microscopes employing lenses made from combinations of both electric and magnetic fields. The current limitations are also discussed in detail along with future improvements.

## Introduction

*Nano material research*, requires observation of surface morphology, fine structures and local elemental distribution of samples. Unlike transmission electron microscopy (*TEM*), scanning transmission microscopy (*STEM*) and atomic force microscopy (*AFM*), scanning electron microscopy (*SEM*) retains a much larger depth of field allowing a greater sense of perspective during characterisation of a material whilst maintaining a high resolution. *SEM* is heavily used in the pursuit of understanding *nano materials* in terms of composition and topographic detail including fine structures since the significant improvement has been made in spatial resolution and detection sensitivities for low voltage electrons in recent years [1].

*SEM* works by demagnifying an electron beam from source to a small probe, which is scanning upon the surface of a sample, and collecting signals emitted from the sample as a function of the sample position.

Here we discuss the signals, secondary electrons

(*SEs*), backscattered electrons (*BSEs*) and characteristic X-rays through energy dispersive (*EDS*) detector. The probe size on the specimen surface, *d*, essentially determines a spatial resolution. Improvement in the performance of *SEM* requires one to: (i) make *d* as small as possible; (ii) separate *SE* and *BSE* signals as far as possible; (iii) enhance *S/N* ratio of the signals; (iv) reduce electron charge up in poorly conductive samples and the subsequent effect on image quality; (v) reduce surface contamination; and (vi) reduce effects of electron irradiation of the sample and subsequent damage.

In this review article, recent improvements of *SEM*, especially performances of JEOL JSM-7401F/7600F and JSM-7100FTTL/7800F concerning to the above mentioned (i–iii), and their outcomes of nano material observation on the (iv & vi) are described.

## Diameter of primary electron (*PE*) on a specimen

The size of electrons source is demagnified through condenser and objective lenses by a magnification factor *M* to a probe at the specimen surface of size *d*. Independent factors such as spherical, chromatic &

---

<sup>1</sup> Daejeon 305-701, Korea, terasaki@kaist.ac.kr

<sup>2</sup> SE-10691 Stockholm terasaki@mmk.su.se

(a) Energy Spectrum of emitted electrons from a sample (b) Classification of various secondary electrons (SEs) and their spatial distribution together with Monte Carlo simulation for Si

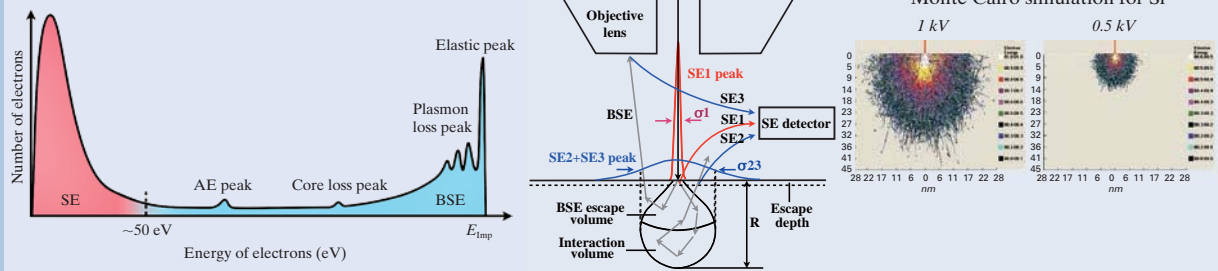


Fig. 1 Schematic diagram of the energy spectrum of emitted electrons from a sample (a), Classification of various secondary electrons (SEs) and their spatial distribution together with Monte Carlo simulation for Si (b). The spatial distribution of SE2 and SE3 is related to the size of BSE escape volume. Spatial distribution of SE1 vs. SE2 and SE3 are schematically shown by red and blue curves, respectively. Full width at half maximums (FWHMs) of SE1 and (SE2 and SE3) are discussed in the papers by Seiler [3] and Cazaux [4]. It is quite clear from Figure 1b that in order to obtain high resolution SEM image irrespective of SEs or BSEs at any landing energies, the best way is to use thin sample with the order of SE escape depth like nano particles on a TEM micro-grid.

diffraction aberrations blur the focus of the probe. The effective size of the probe of primary electrons (PEs) impacting on the surface on a sample,  $d$ , is given by the following equation using conventional parameters: [2]

$$d^2 = \sqrt{d_0^2 + d_d^2 + d_s^2 + d_c^2}$$

$d_0$ ,  $d_d$ ,  $d_s$ , and  $d_c$  are contributions to the disc of least confusion from source size, diffraction, spherical aberrations, and chromatic aberration, and these are expressed thusly:

$$d_0 = \frac{2}{\pi\alpha} \cdot \sqrt{\frac{I_p}{\beta}}$$

$$d_d = \frac{0.6\lambda}{\alpha}$$

$$d_s = 0.5C_s\alpha^3$$

$$d_c = C_c \frac{\Delta E}{E}\alpha$$

Where:  $I_p$  = PE beam current;  $\beta$  = brightness of electron source;  $\alpha$  = PE convergence angle at sample position;  $\lambda$  = the wavelength of the PE at the sample;  $C_s$  = spherical aberration constant;  $C_c$  = chromatic aberration constant;  $\Delta E$  = energy spread of electron source; and  $E$  = landing energy (landing voltage) at the sample, respectively.

Electrons of various types are emitted from the irradiated volume (interaction volume) and their energy spectrum is schematically shown in **Figure 1a**. Emitted electrons are conventionally classified as BSEs or SEs with electron energy larger or smaller than 50 eV, respectively.

Higher spatial resolution is principally achieved by reducing the diameter of a PE beam ( $d$ , see Figure 1b), and/or reducing the signal generation volume (the area of the interaction volume where detectable electrons are emitted). Reduction of the impact electron energy (landing energy) onto a specimen, will reduce the signal generation volume region and also limit electron radiation damage and electron charging problems in electrically insulating materials. However, the associated increase in probe size and loss of resolution therefore drives new improvements

of an objective lens both in making the effective probe size  $d$  small based on the above equation and enhancing detection sensitivity. Furthermore, emitted electrons containing morphological and compositional information of the sample require separation or superimposed if necessary by selecting energy of signal electrons. Considering these things, reducing diameter of PE on a specimen at low landing energy and energy selections of signal electrons are of extreme importance.

PEs change their directions once impacting with the sample surface through elastic and inelastic scattering inside a specimen. As SEs have kinetic energy smaller than 50 eV, and the associated limited escape depth means only SEs close to the specimen surface are emitted. The escape depth is approximately 5 times the mean free path of SEs. The mean average escape depth is 0.5~1.5 nm for metals and 10~20 nm for insulators. [3] SE1s and SE2s are generated by PEs and BSEs, respectively. SE3 are generated outside the specimen by BSEs hitting a pole piece and/or chamber walls (Figure 1b). Obtaining surface structural information in high resolution requires selection and enhancement of SE1 collection since SE1 has high special information having been emitted near the impact point of PEs, SE2s and SE3s carry information from the interaction volume through BSEs. Unfortunately, SE detectors cannot distinguish SE1s from SE2s and SE3s producing an SE image of SE1 information superimposed with BSEs information of lower resolution. A reduction in the landing energy of PEs, will reduce the signal generation volume of BSEs resulting in SE2 and SE3 electrons of higher spatial resolution. High resolution SE and BSE images can therefore be obtained with low landing energy PEs as well as BSE image.

A combination of magnetic lens and retarding electrostatic field had been used from the early stages of SEM [5]. In 1981, Yau *et al.* investigated an objective lens combining a magnetic field with a retarding electrostatic field to reduce the diameter of the PE, [6] (electromagnetic lens). Combining these fields makes the lens effectively stronger with a comparatively shorter focal length. Therefore, aberrations of the electromagnetic lens are smaller than those of purely

magnetic and purely electrostatic lenses. Various types of electromagnetic lenses have been proposed and realized. [7] The substrate negative bias (also called *sample bias*) with respect to objective lens for conventional purely magnetic lens makes the objective lens an electromagnetic lens, since an electrostatic retarding field is generated between the magnetic lens and the sample, and this field acts as a focusing field for primary electrons. This is especially valuable for low energy *PEs*, since lens effect of electrostatic field is strong for low energy *PEs* and furthermore reduces both *Cs* and *Cc* values. This electrostatic field also acts as an accelerating field for signal electrons from a sample, which is used as a part of detection system as described later.

Using sputtered gold nanoparticles on carbon, the dependence of *SEM* image resolution on specimen bias is shown in **Figure 2** by keeping landing energy constant at 500 eV. It is clearly observed that the resolution of the *SEM* image has been greatly improved with increase of specimen bias from 0 to -5 kV.

Schematic diagram and typical trajectories of *SEs* (blue) and *BSEs* (red) for JSM-7401F/7600F are shown in **Figures 3a-d**, respectively. In the detection system of 7401F/7600F, there are several electrodes to select signal electrons. This detection system is called r-filter. Acceleration electrode (*AE*) acts as energy filter: high energy *BSEs* always go through it, but transmission of low energy *SEs* depends on bias voltage of *AE* (Figure 3b-d). When *AE* is biased in positive, *SEs* can go through it (Mode *SE* (Figure 3b) and Mode *Sb* (Figure 3d)), but when it is negative, *SEs* cannot go through it (Mode *BSE* (Figure 3c)). In Mode *SE*, *SEs* are effectively collected by the electric field produced by middle electrodes (*MEs*) as described in Figure 3b, while *BSEs* hit the reflector electrode (*RE*) and generate *SEs* (*SE3s*), but these *SE3s* are trapped by positively biased *RE* resulting in selective detection of *SEs*. In *BSE* mode (Figure 3c), *SEs* emitted from a sample are reflected by *AE*, while *BSEs* hit the reflector electrode, and generate *SEs* (*SE3s*). These *SE3s* are collected by Secondary Electron Detector (*SED*) thanks to negative bias to *RE* and *MEs*. In Mode *Sb*, combination of these are applied, and *SEs* and *BSEs* are successfully detected (Figure 3d).

Schematic diagram and typical trajectories of an electrons for JSM-7100F TTL/7800F are shown in **Figures 3e and f**, respectively. Without strong electrostatic field between a magnetic lens and a substrate generated by substrate bias, trajectory of *BSEs* are rather straight, which makes most *BSEs* not going into *SEM* column (Figure 3e). Thus, a conventional high efficiency *BSE* detector (*BED*) should be placed between a substrate and a magnetic lens (Figure 3e), making both the working distance and the focal length long, and degrading the diameter of *PE*. When a bias voltage is applied to the specimen substrate, an electrostatic field is produced between the magnetic lens and substrate (bi-potential lens), allowing the diameter of *PE* to be small even at low landing energy, as described above. In addition, the substrate bias changes trajectory of *BSE*: trajectory is almost parabolic near the substrate, and directions of *BSEs* are modified to upwards, making them go into the *SEM* column (Figure 3f). Furthermore, these *BSEs* are accelerated by the electric field, which makes detection of these *BSEs* easy. These enable detection of *BSEs* inside the column with a shorter working distance and a small diameter of *PE* even at low landing energy of

impact electrons as well as the effect of electromagnetic lens. Thus we have overcome traditional problems in *BSE* image. Since JSM-7800F has energy filter inside *SEM* column, simultaneous detection of *BSE* and *SE* is possible (Figure 3e and f). This simultaneous imaging is especially valuable for electron beam sensitive materials, mixed phases / compounds with characteristic nano-feature and different composition and so on.

Here we describe the recent experimental results obtained by JSM-7401F/7600F and JSM-7100F TTL/7800F with specimen bias (Gentle Beam (GB) mode).

## Electron beam damage and fine structures from electron beam sensitive materials (Zeolites, meso-zeolite LTA & MOF)

### a) SEM and atomic force microscopy (AFM) images of STA-7 and LTA.

Crystal surfaces of two zeotype crystals, LTA and STA-7, were oriented orthogonally with respect to the electron-optic axis of the *SEM* and irradiated with an electron probe of various doses and energies using JSM-7401F. [8] This produced rectangular areas of contrast, corresponding to the scanned area of interest, when viewed from a lower magnification (**Figure 4c**) that were absent before irradiation (Figure 4b). The rectangular areas were analyzed *ibidem* (in the same place) by atomic force microscopy (*AFM*). Areas with very low electron exposure possess a rectangular contrast in the *SEM* but exhibit a zero height depression as measured by *AFM*. This establishes that contrast from contamination, another contributor to loss of information in a *SEM* image, is still present even at nondestructive electron doses. The depth increased with increasing time of electron exposure and increasing probe current to an eventual maximum depression of just under 20 and 15 nm for STA-7 and LTA, respectively, with the former crystals exhibiting a more rapid collapse (Figure 4a, d, and e). In both materials, the nanometer surface terraces are preserved with no discernible distortion in the irradiated area (Figure 4g-j). Figure 4i and j illustrates how the *AFM* cross section in Figure 4g and h is the result of translation of the surface in a direction orthogonal to the crystal face.

The measured step heights within the damaged area differ by less than 5% (i.e., within the precision limit of the *AFM*) when compared to the step heights outside of the damaged area. The lack of distortion of the crystal surface, when measured by *AFM*, is therefore surprising. This implies that the area of the crystal experiencing crystalline-amorphous (*C-A*) transitions is sufficiently below the surface to leave it geometrically unaltered. *SEs* contribute to topographic contrast in the *SEM* as their escape depth is no more than 10 nm. The majority of impact electrons penetrate much deeper into the interaction volume. The inelastic collisions are responsible for the *C-A* transitions, and because they occur mainly at sufficient depth, the surface remains chemically and structurally intact.

### b) Meso LTA (at different impact energies)

In recent years, zeolite crystallization studies were

## Dependence of SEM image on specimen bias

Landing voltage = 500 V

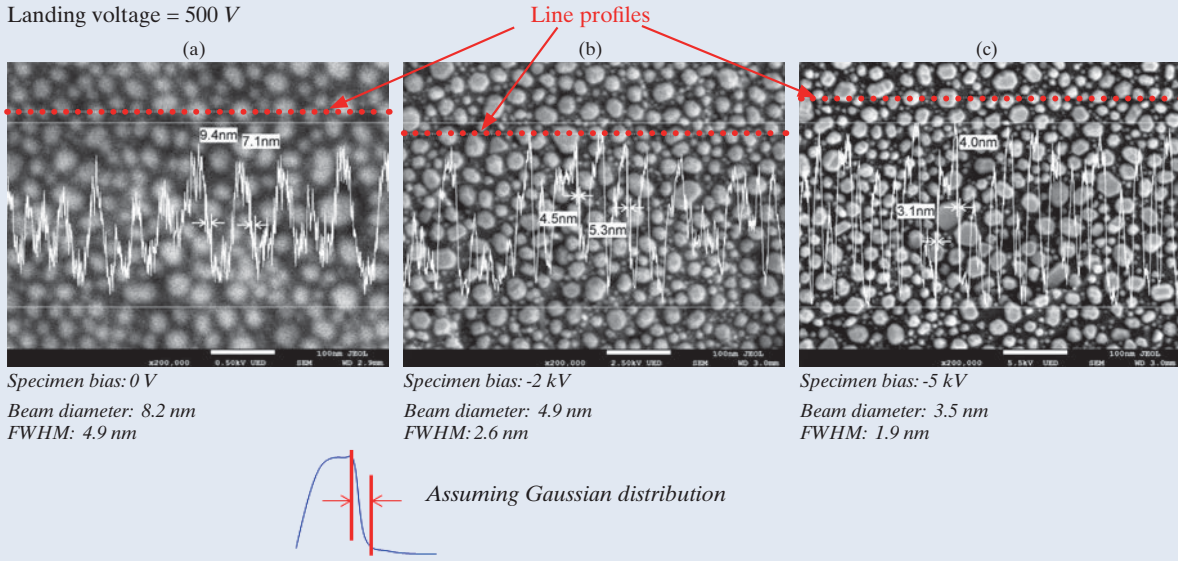


Fig. 2 SEM resolution dependency on substrate bias. With increasing substrate bias from 0V (a) to -5 kV (c), resolution improves. These images are taken using JSM-7800F with GBSH (Gentle Beam Super High resolution) option allowing specimen bias (absolute value) up to -5 kV.

## Schematic diagrams and typical trajectories of SEs and BSEs for JSM-7401F/4600F and JSM-7100FTTL/7800F

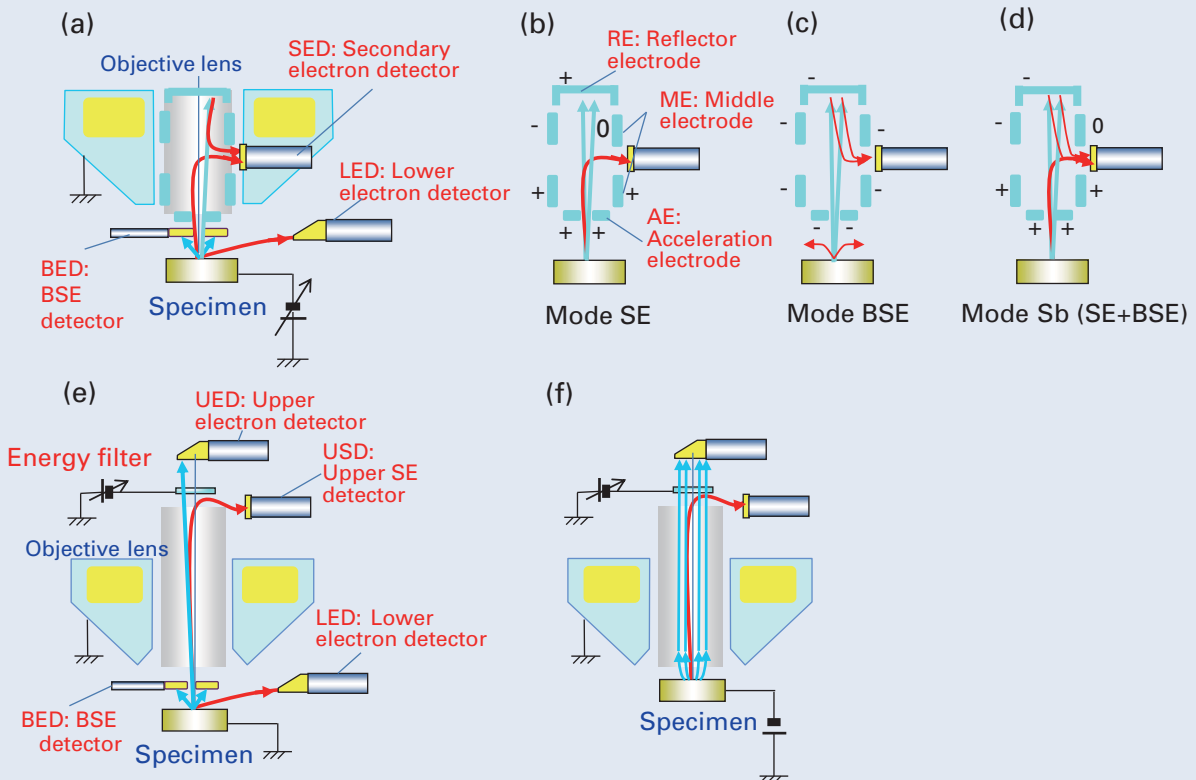


Fig. 3 Schematic diagram and the typical trajectories of SEs and BSEs for JSM-7401F/7600F (a-d) and JSM-7100F/7800F (e, f). SEs and BSEs are selectively detected using electrodes or energy filter.

## AFM study of nanoscale e-beam damage under HRSEM observation

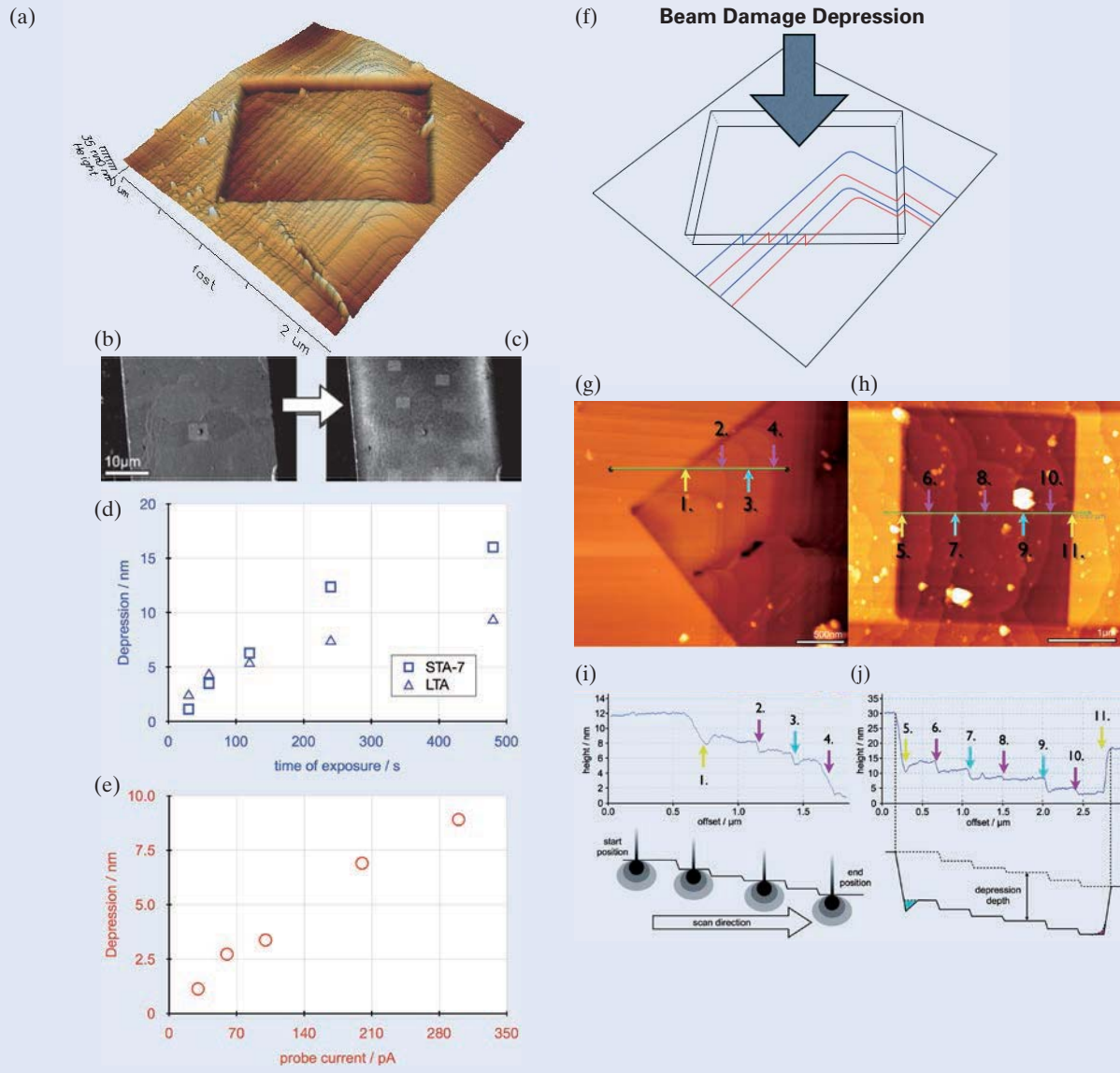


Fig. 4 AFM study of nanoscale e-beam damage under HRSEM observation. AFM image after HRSEM observation (a) and schematic drawing (f). Low magnification SEM image before (b) and after (c) HRSEM observation. Depression of a surface by e-beam damage depending on time of exposure (d) and depending on probe current (e). Depression of a surface depending on various conditions (g-j).

## E-beam damage comparison at extreme low voltage on mesoporous LTA

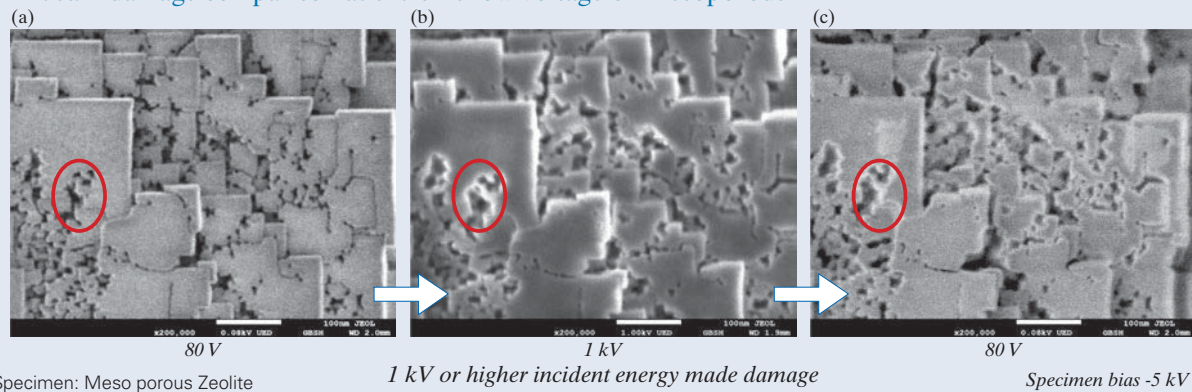


Fig. 5 E-beam damage comparison at extreme low voltage on mesoporous LTA. SEM image taken at extreme low landing voltage of 80 V before observation at 1 kV (a), SEM image taken with landing voltage of 1 kV (b), and SEM image at landing voltage of 80 V after observation at 1 kV. Specimen bias of -5 kV allows high resolution images even at landing voltage of 80 V.

mostly focused on nanocrystalline zeolites with particle diameters less than 50 nm and hierarchically porous, micro-, meso- and macro-porous zeolites. LTA zeolite with mesopores was successfully synthesised by Ryong Ryoo's group under a hydrothermal synthesis condition that contained a quaternary ammonium-type organosilane surfactant and their mesopore architectures were reported previously by *LV-HRSEM* combined with Cross-section polisher (*CP*) sectioning [9]. The *HRSEM* investigation revealed presence of a disordered network of mesoporous channels that penetrated the microporous zeolite crystal. Here we show the effect of electron beam energy on damage at very low landing energies. **Figure 5a, b and c** were taken in sequence with time at landing voltage of 80 V, 1 kV and 80 V, respectively. Especially, the image of 80 V shows less edge effect due to small interaction volume. That is a good feature of low voltage *HRSEM* (*LV-HRSEM*), because it shows fine edges and gives highly accurate measurement of nano porous materials. Moreover, there are damages due to electron beam irradiation as large gap on the Figure 5b, which are indicated with circle. On the other hand, Figure 5a and c show no or less damages by electron beam.

These clearly show the importance of using low landing energy for electron beam sensitive materials.

### c) IRMOF-74

Isorecticular series of MOF-74 structures (termed IRMOF-74-I to XI) with pore apertures ranging from 1.4 to 9.8 nm has been successfully synthesised by Omar Yaghi's group [10]. When unit-cell size of crystals become larger, it becomes hard to obtain even unit cell parameters by powder X-ray diffraction (*XRD*) patterns because of serious overlap of reflections and sever damping of intensity with

increase of scattering vectors. Furthermore confirmation of non-existence of surface barrier is becoming important to utilise the pores of materials. **Figure 6a** is schematic drawing of IRMOF-74-VII and **Figure 6b** shows *TEM* image. A JEM-2010F field emission *TEM* equipped with a CEOS post-specimen spherical aberration corrector (Cs corrector) was operated at 120 kV for high-resolution transmission electron microscopy (*HRTEM*) imaging. Since MOF materials are electron beam sensitive, the electron beam damage to the specimen was minimized as much as possible (in this study, the beam density during the observations was from 50 to 130 electrons/(nm<sup>2</sup>)). A single *HRTEM* image with an exposure time of 2 seconds or a sequence of images (10 frames) was recorded, with a 0.5 second exposure time for each frame and after drift compensation, some frames can be superimposed to increase the signal-to-noise ratio (*S/N*) for display.

**Figure 6c** was taken from IRMOF-74-VII at landing voltage of electron 300 V (Acceleration voltage = 5.3 kV, the specimen bias = - 5.0 kV, Beam current = 2.0 pA), and showed clearly pores with diameter of ~ 3.5 nm and hexagonal arrangement of them. A substrate bias of -5.0 kV was achieved with newly developed *GBSH* (Gentle Beam Super High resolution) option for JSM-7800F.

As the MOFs and Zeolite research expand more and more to nano scale, utilisation of *EM* method becomes imperative, since *XRD* on crystals of nano size will not be sufficient to characterise their structures any more. So the *EM* method plays important roles in characterisation of Zeolites and MOFs that has at least one dimension fall into nano scale. These include nano particles, nano rods, nano ribbons, nano sheet, nano films, to just name a few. As the resolution of *EM* methods improves, more structural detail can be observed in the crystals of MOFs and Zeolites. The evolution of *EM* technology will

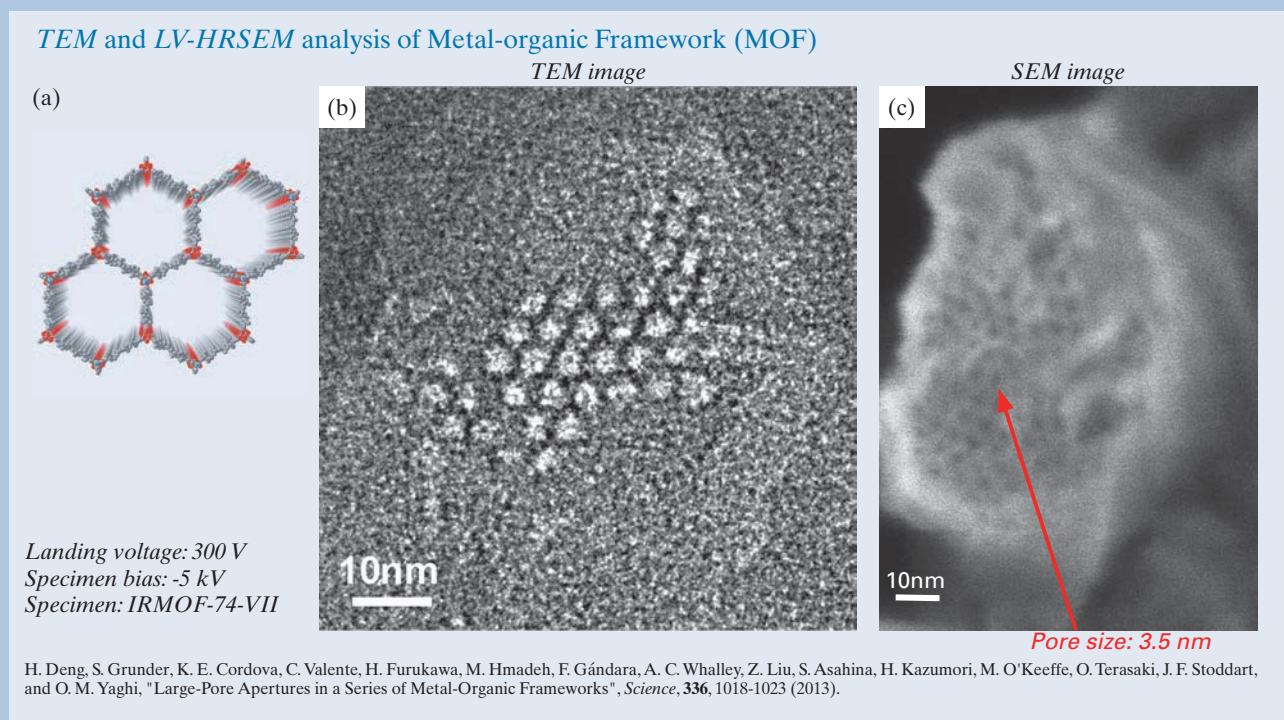


Fig. 6 Analysis of Metal-organic Framework (MOF). Schematic drawing (a), *TEM* image (b), and *SEM* image (c) of MOF. Pores with diameter of 3.5 nm are clearly observed in *TEM* image (b) and *SEM* image (c).

definitely change the way of traditional characterisation of materials where only space average of the crystal lattice counts, but rather by providing direct and real time view of a crystal surface with a few nanometer thickness. In short, *EM* methods are 1. good for nano sized MOF; 2. good for structural details; and 3. provide dynamic information.

## Improved LV-HRSEM images

### (a) Helical $\text{TiO}_2$

Very recently, chiral  $\text{TiO}_2$  nanofibres with electron transition-based optical activity have been synthesised by Shunai Che's group by the transcription of the helical structure of amino acid-derived amphiphile lipid enantiomers through coordination bonding interactions. The as-prepared lipid- $\text{TiO}_2$  hybrid was exclusively composed of right/left-handed double-helical amorphous  $\text{TiO}_2$  fibres with  $\sim 25 \text{ nm}$  in width and  $\sim 100 \text{ nm}$  pitch length along the fibre axis and the fibres possess inner tubular structures with diameter of  $\sim 12 \text{ nm}$  along their central axes. The chemical composition and the structure made the *SEM* observation of such material very difficult. To reduce

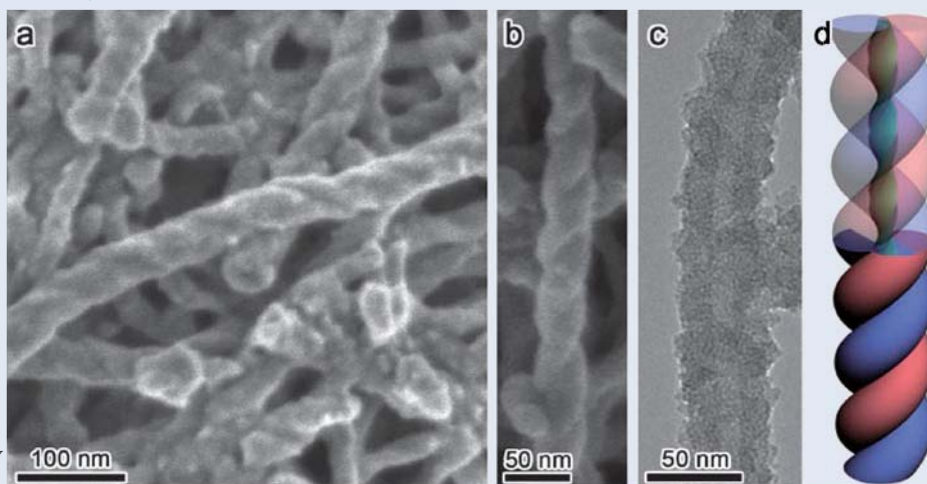
the probe size and the interaction volume to achieve high resolution,  $0.5 \text{ kV}$  landing voltage with  $-2.0 \text{ kV}$  bias voltage applied to the specimen substrate and a short working distance of  $3.0 \text{ mm}$  were used and the detail morphology of the fibres were nicely revealed (**Figure 7a** and **b**). The *HRTEM* image and the corresponding model are shown in **Figure 7c** and **d**, respectively.

The as-prepared amorphous hybrids can be converted to crystalline  $\text{TiO}_2$  with stacks of anatase nanocrystals with of  $\sim 20 \text{ nm}$  size by calcination, which is shown in **Figure 7e**. Compared to as-prepared sample, higher landing voltage of  $1.0 \text{ kV}$  with  $-2.0 \text{ kV}$  bias voltage and a shorter working distance of  $2.6 \text{ mm}$  were used. **Figure 7f** shows a *HRTEM* image of an array of nanocrystals exhibits the contrast close to  $\langle 111 \rangle$  zone axis of the anatase structure, particularly, the adjacent nanocrystals have a rotational misplaced arrangement, piling up by sharing one of their  $\{101\}$  facets while keeping one of the  $\langle 111 \rangle$  axis in common, leading to a helical array of nanocrystals with almost parallel  $\langle 111 \rangle$  axes (**Figure 7g**). However, it is very difficult to determine the structural relationship of all the nanocrystals due to the overlapping problem and the small crystal size.

### TEM and LV-HRSEM analysis of Helical $\text{TiO}_2$

*LV-HRSEM*  
for as synthesised

Landing voltage:  $0.5 \text{ kV}$   
Specimen bias:  $-2 \text{ kV}$



*LV-HRSEM*  
for as calcined

Landing voltage:  $1 \text{ kV}$   
Specimen bias:  $-2 \text{ kV}$

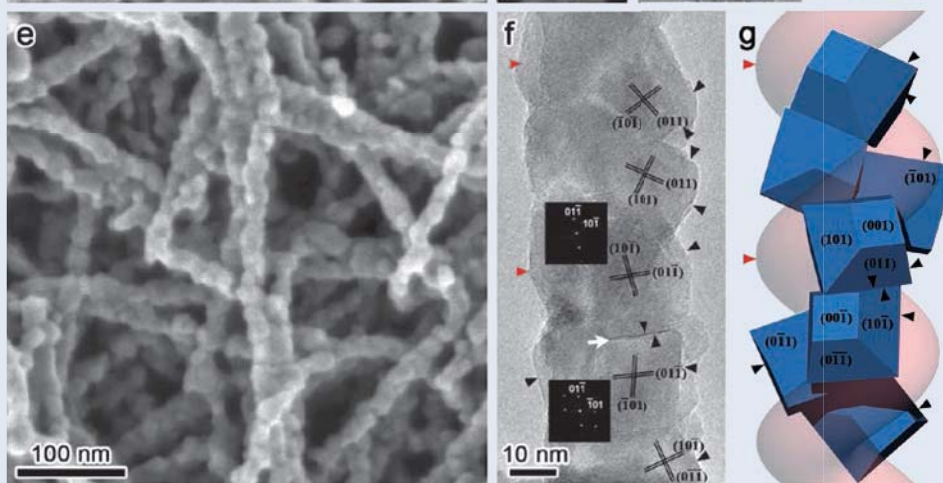


**Fig. 7** *LV-HRSEM* images taken with landing voltage of  $0.5 \text{ kV}$  with the specimen bias of  $-2.0 \text{ kV}$  (**a** & **b**), *HRTEM* image (**c**) taken at  $200 \text{ kV}$  and the schematic drawing (**d**) of the as-prepared organic lipid- $\text{TiO}_2$  hybrid fibres; The *LV-HRSEM* image taken with landing voltage of  $1.0 \text{ kV}$  with the specimen bias of  $-2.0 \text{ kV}$  (**e**), *HRTEM* image taken at  $200 \text{ kV}$  (**f**) and the schematic drawing (**g**) of calcined chiral crystalline  $\text{TiO}_2$ .

From these results, we may suggest that the crystallization process is formed locally according to the initially formed double-helical structures while generally retained the double-helical morphology of the as-prepared samples, however, the hollow tubular structures disappeared. Both the amorphous and anatase crystalline helical  $\text{TiO}_2$  fibres exhibited optical response to circularly polarized light at the absorption edge around  $\sim 350 \text{ nm}$ . This was attributed to the semiconductor  $\text{TiO}_2$ -based electronic transitions from the valence band to the conduction band under an asymmetric electric field [11].

### (b) Porous crystals with different length scales (SBA-15)

Mesoporous silica crystal, SBA-15, has  $2d$ -hexagonally arranged primary mesopores (channels) with plane group  $p6mm$ . The crystal has a highly complex porosity with, in addition to the main mesopores, unordered pores penetrating the amorphous silica wall. These intrawall pores have a broad size distribution, from micropores to small mesopores. As a consequence of the formation sequence, the main mesopores contain to varying degree

“plugs” that may or may not seal the mesopore to the exterior, i.e. the mesopores may not be accessible to chemical reagents or probing gas molecules. Although nitrogen sorption generally provides valuable information on the porous character of mesoporous materials it is only by direct observation that detailed information on the porosity can be unveiled. To be able to understand the growth process, gas adsorption/ desorption processes and to be able to efficiently functionalize the pore walls there is a need to properly characterize these complicated structures, including pore openings and the accessibility. In order to observe *HRSEM* image of electric non-conductive silica mesoporous crystals free from the electron-charging problem, we need to use *LV-HRSEM* by improving its resolving power in low impact energy as mentioned before. [12] *SE* images are taken exactly same area at specimen bias  $= -2 \text{ kV}$  and  $-5 \text{ kV}$  keeping both landing voltage  $300 \text{ V}$  and beam current  $5.5 \text{ pA}$ , are shown in **Figure 8a** and **b**. It is clear that resolution and *S/N* are greatly improved by increasing bias voltage. Micropores in channel walls as well as plugs inside channels are observed in **Figure 8c**. Contaminations on the sample accumulated during observation were successfully removed by Ar-ion

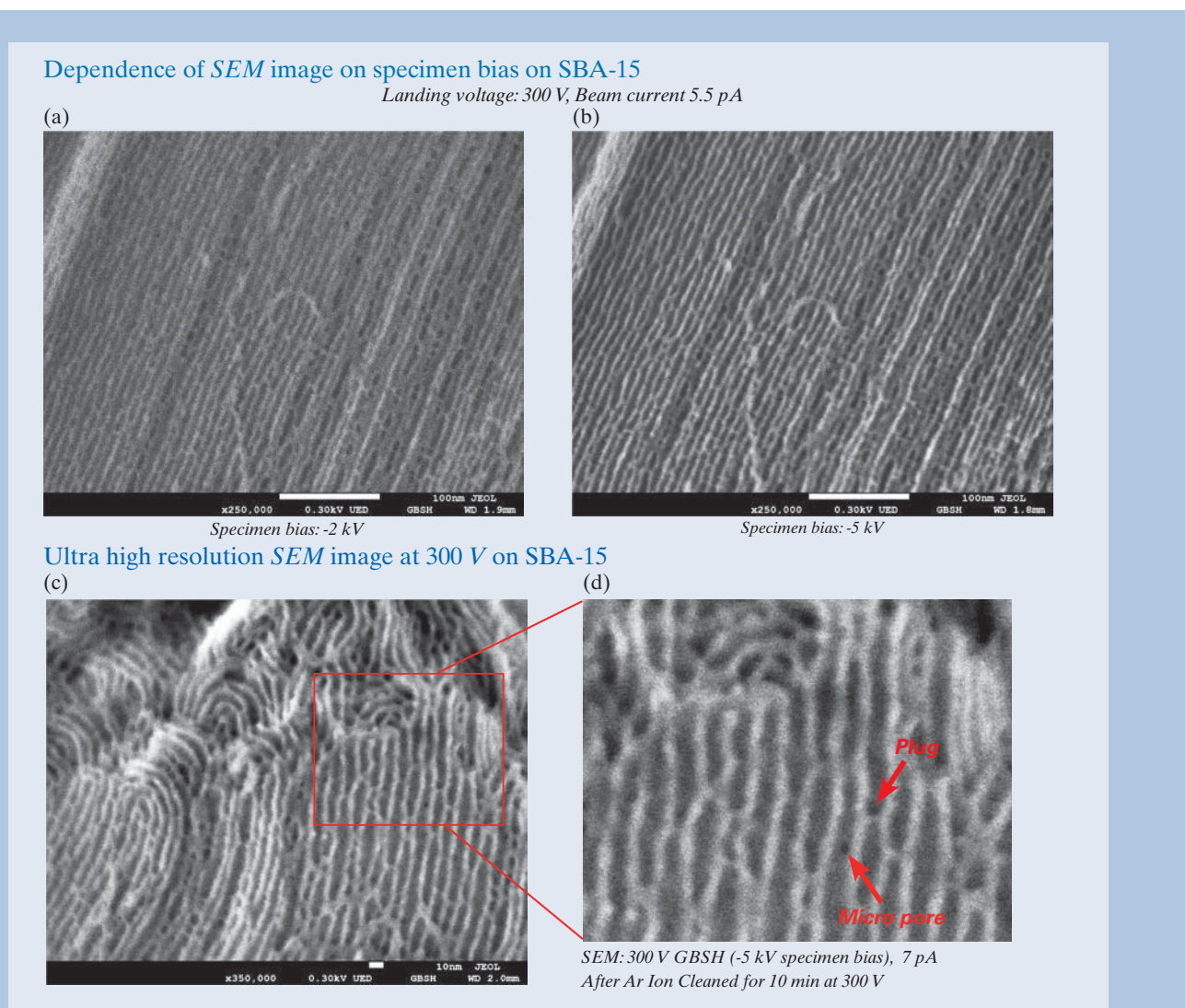


Fig. 8 SEM images of SBA-15 at landing voltage of 300 V. Specimen bias of  $-2 \text{ kV}$  (a) and  $-5 \text{ kV}$  (b-d). Increase of specimen bias voltage (absolute value) improves both resolution and *S/N* of *SE* image of SBA-15 (a, b). Micropores are clearly observed (c, d).

as shown in Figure 8d.

### (c) Gold yolk-shell materials, Au@TiO<sub>2</sub>, Au@ZrO<sub>2</sub> and Au@C

Gold yolk-shell materials, Au@TiO<sub>2</sub>, Au@ZrO<sub>2</sub> and Au@C, have been synthesised through nanocasting of Au nanoparticles in TiO<sub>2</sub>, ZrO<sub>2</sub> and Carbon spherical shells with

pores via silica route, that is Au@SiO<sub>2</sub>@X (where X=TiO<sub>2</sub>, ZrO<sub>2</sub> and Carbon) and SiO<sub>2</sub> core is selectively removed with aqueous NaOH. This structure allows efficient stabilization of the metallic cores at high temperature conditions, while maintaining high catalytic activity through not only intrinsic catalytic activity of gold nanoparticles but also supports. The high structurally and compositionally defined yolk-shell particles make these kinds of material ideally suited by discriminating effects of support and particle-size for

#### Nano Structural analysis using TEM on Au@TiO<sub>2</sub>

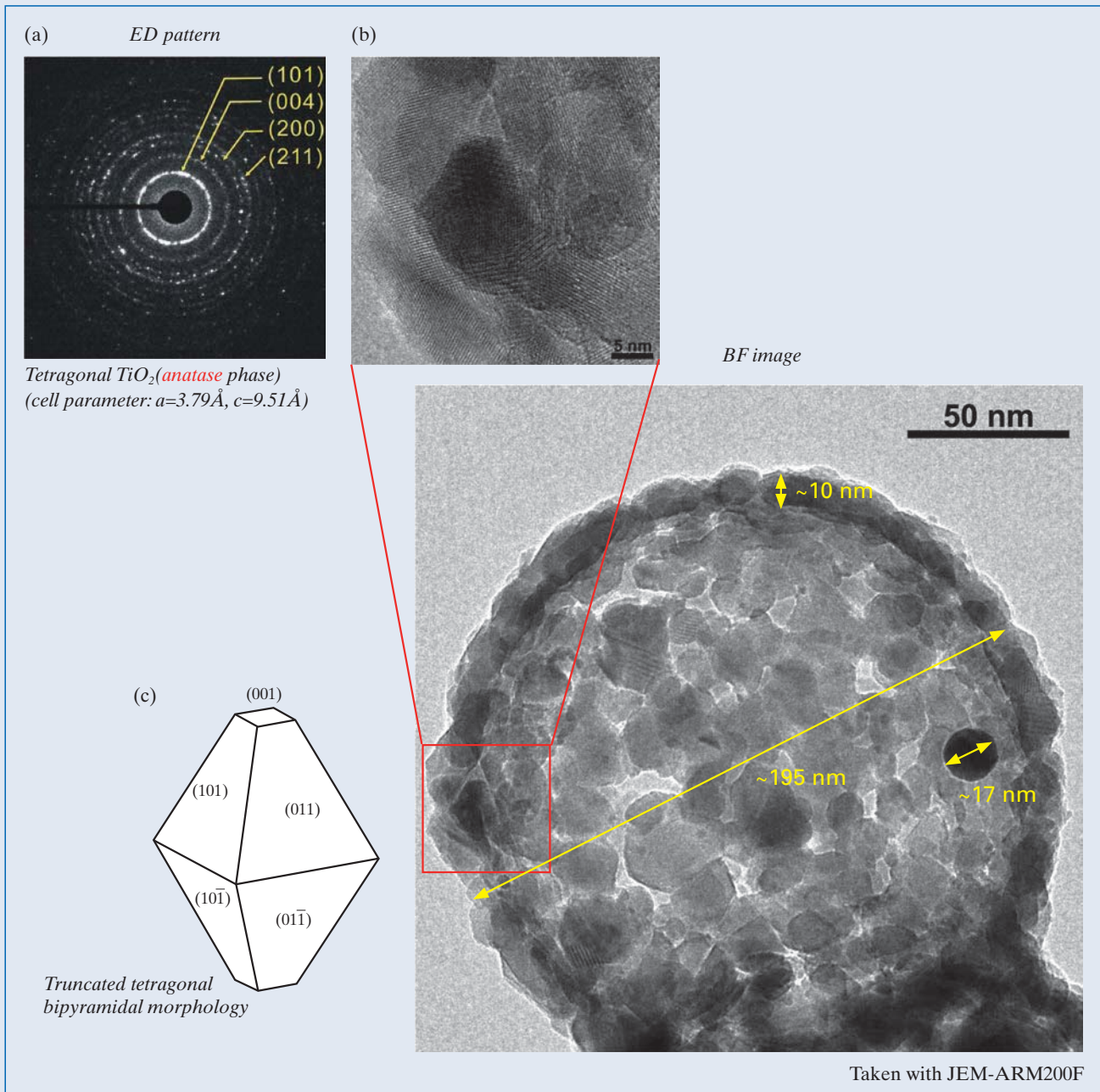


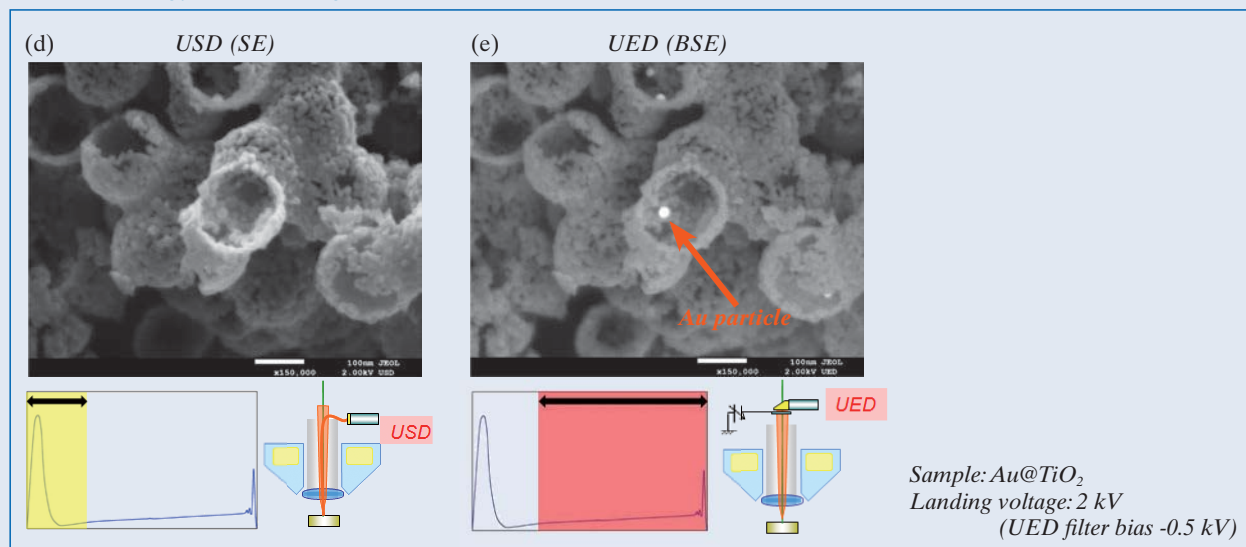
Fig. 9 Au@TiO<sub>2</sub>, Nano Structural analysis using TEM on Au@TiO<sub>2</sub> (a-c), electron energy filtered SEM images providing mainly SE (d) and BSE (e) information, improved resolution of BSE with sample bias (f-h).

mechanistic studies in heterogeneous catalysis [13]. Here results only on Au@TiO<sub>2</sub> are shown. Electron diffraction (ED) pattern and high resolution TEM bright field (BF) image taken with JEM-ARM200F are shown in **Figure 9a** and **b**. These show that TiO<sub>2</sub> is anatase structure, TiO<sub>2</sub> crystal sometime shows nice truncated tetragonal bipyramidal morphology, and that gold particle has spherical shape with diameter *ca* 17 nm (multiply twined particles are also found in other york-shells).

Electron energy filtered images are taken from Au@TiO<sub>2</sub> at electron landing voltage= 2 kV. USD and UED collect electrons with low and high energy, corresponding mostly to SEs, and BSEs, respectively, when UED energy filter bias is set at - 500 V. We can obtain images simultaneously by USD and UED, and can confirm that USD gives topological contrast while UED gives Z contrast.

It is confirmed as expected that resolution of BSEs

### Electron energy filtered images Au@TiO<sub>2</sub>



### GB mode improves spatial resolution for LV-BSE

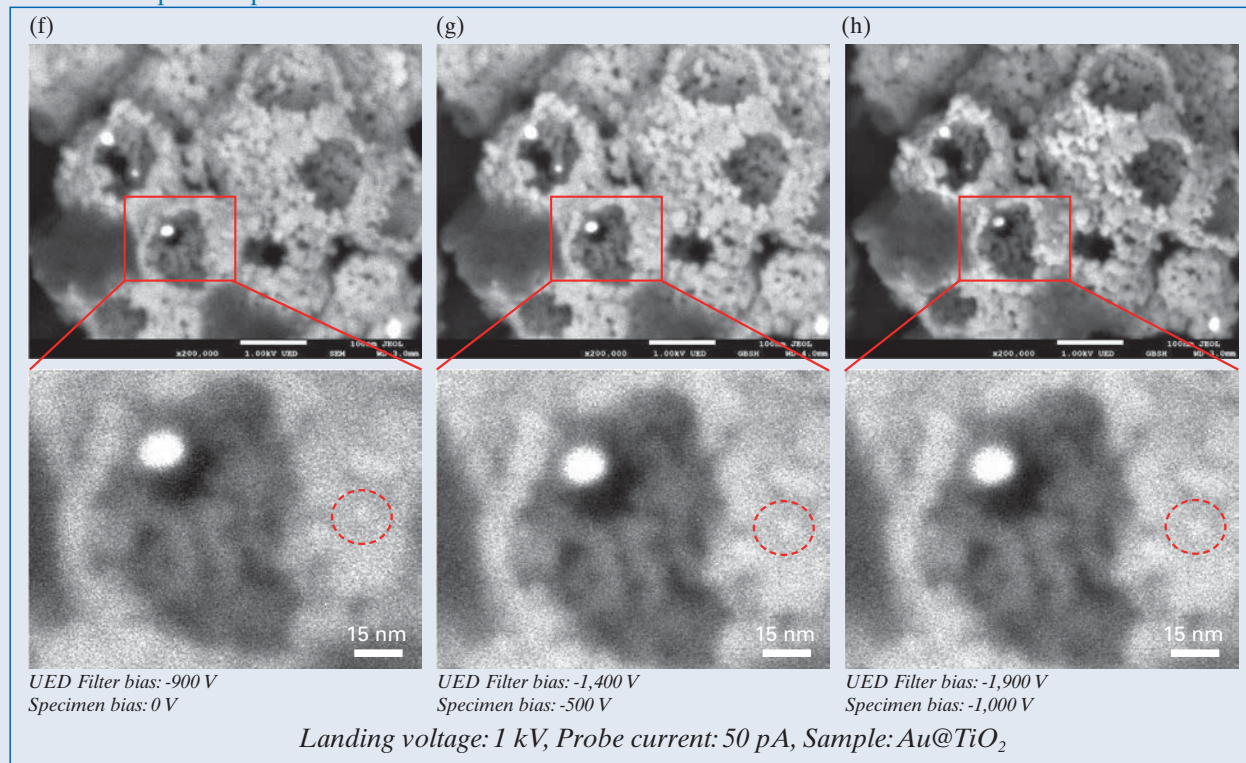


image obtained with *UED* is improved by loading specimen bias keeping landing voltage and beam current constant (1 kV and 50 pA, respectively) Figure 9f-h.

*BSE* image (Figure 10a) and *EDS* mappings (Figure 10b and c) are shown. Resolution of *EDS* mapping is greatly improved by placing specimen bias from 0 (Figure 10b) to -5 kV (Figure 10c) at landing voltage of 4 kV. Resolution of *EDS* mapping is usually dominated by signal generation volume, but in this case, diameter of *PE* affects resolution.

## Conclusion and future progress

Since our last publication in *JEOL News* [1] on high resolution scanning electron microscopy we have seen limitations broken in the resolution of both topographic and compositional information. Whereas previous breakthroughs were down to computer aided design, this time, that design has been directed towards more optimum combinations of electric and magnetic lenses facilitating further progress. However, there is no direct indication that current configurations and associated conditions and parameters have reached a universally recognised minima. There are many other exciting advances through use of ultra low energy work done, the high energy work done on thin samples and low-loss energy electrons (plasmon-loss).

## Acknowledgments

Financial support from VR & Knut Alice Wallenberg Foundation and EXSELENT (Sweden), JST (Japan), WCU (R-31-2008-000-10055-0) and IBS (Korea) are acknowledged.

## References

- [ 1 ] Stevens et al., *JEOL News* & Liu et al. A review of fine structures of nanoporous materials as evidenced by microscopic methods. *J Electron Microscopy* **vol. 62** pp.109-145 (2013).
- [ 2 ] Asahina et al. A new HRSEM approach to observe fine structures of novel nanostructured materials. *Mesoporous and Microporous Materials* **vol. 146** pp. 11-17 (2011).
- [ 3 ] Seiler, Secondary electron emission in the scanning electron microscope, *Journal of Applied Physics* **vol. 54** pp. R1-R18 (1983).
- [ 4 ] J. Cazaux. About the role of the various types of secondary electrons (SE1; SE2; SE3) on the performance of LVSEM, *Journal of Microscopy* (2004) vol. 214 pp. 341-347.
- [ 5 ] Paden and Nixon, Retarding field scanning electron microscopy. *J. of Scientific Instruments* **vol. 1** p.1073 (1968).
- [ 6 ] Yau et al. Generation and applications of finely focused beams of low-energy electrons. *Journal of Vacuum Science and Technology* **vol.19** pp.048-1052 (1981).
- [ 7 ] Frosien et al. Compound magnetic and electrostatic lenses for low-voltage applications. *International symposium on electron, ion, and photon beams* **vol. 7** pp.1874-1877 (1989); Yonezawa et al. Single pole-piece objective lens with electrostatic bipotential lens for SEM. *Journal of Electron Microscopy* **vol. 51** pp.149-156 (2002); Khurshed, A. Ultimate resolution limits for scanning electron microscope immersion objective lenses. *Optik - International Journal for Light and Electron Optics* **vol. 113** pp.67-77 (2002).
- [ 8 ] Stevens et al. Nanoscale Electron Beam Damage Studied by Atomic Force Microscopy. *J. Phys. Chem.* **vol. C113** pp. 18441-18443 (2009).
- [ 9 ] Cho et al. Mesopore generation by organosilane surfactant during LTA zeolite crystallization investigated by high-resolution SEM and Monte Carlo simulation. *Solid State Sciences* **vol. 13** pp. 750-756 (2011).
- [10] Deng et al. Large pore apertures in a series of metal-organic frameworks. *Science* **vol. 336** pp. 1018-1023 (2012).
- [11] Liu, S. et al. Synthesis of chiral TiO<sub>2</sub> nanofibre with electron transition-based optical activity. *Nat. Comms.* **vol. 3**, p.1215 (2012).
- [12] Kjellman et al. Independent fine-tuning of the intrawall porosity and primary mesoporosity of SBA-15, *Chem Mat* **vol 25**, pp1989-1997., and Kjellman et al. submitted (2013).
- [13] C. Galeano et al. Yolk-Shell Gold Nanoparticles as Model Materials for Support-Effect Studies in Heterogeneous Catalysis: Au, @C and Au, @ZrO<sub>2</sub> for CO Oxidation as an Example. *Chem. Eur. J.* **vol.17** pp.8434-8439 (2011).

